

InGaP  $2 \times 2$  pixel array for X-ray and  $\gamma$ -ray spectroscopyS. Butera<sup>a</sup>, G. Lioliou<sup>a,\*</sup>, S. Zhao<sup>a</sup>, A.B. Krysa<sup>b</sup>, A.M. Barnett<sup>a</sup><sup>a</sup> Space Research Group, School of Mathematical and Physical Sciences, University of Sussex, Brighton, BN1 9QT, UK<sup>b</sup> EPSRC National Epitaxy Facility, University of Sheffield, Mappin Street, Sheffield, S1 3JD, UK

## ARTICLE INFO

## Keywords:

InGaP

X-ray photon counting spectroscopy

 $\gamma$ -ray photon counting spectroscopy

Pixel array

## ABSTRACT

A  $2 \times 2$  square pixel  $\text{In}_{0.5}\text{Ga}_{0.5}\text{P}$  p<sup>+</sup>-i-n<sup>+</sup> mesa photodiode array was fabricated and investigated for its suitability in photon counting X-ray and  $\gamma$ -ray spectroscopy. Each pixel, which had an area of  $200 \mu\text{m} \times 200 \mu\text{m}$  and a  $5 \mu\text{m}$  thick i layer, was coupled to a low-noise charge-sensitive preamplifier and standard onwards readout electronics to form an X-ray and  $\gamma$ -ray photon counting spectrometer. The pixels were illuminated in turn with an  $^{55}\text{Fe}$  radioisotope X-ray source, an  $^{241}\text{Am}$  radioisotope X-ray and  $\gamma$ -ray source, and a  $^{109}\text{Cd}$  radioisotope X-ray and  $\gamma$ -ray source. The mean value (across all pixels) of the best energy resolution (Full Width at Half Maximum, FWHM) at  $20^\circ\text{C}$  was  $770 \text{ eV} \pm 30 \text{ eV}$  at  $5.9 \text{ keV}$ ,  $840 \text{ eV} \pm 20 \text{ eV}$  at  $22.16 \text{ keV}$ , and  $870 \text{ eV} \pm 30 \text{ eV}$  at  $59.54 \text{ keV}$ . The spectroscopic response of one of the pixels was then investigated at temperatures up to  $100^\circ\text{C}$ ; noise analysis was performed and the different noise contributions were identified. The FWHM at  $100^\circ\text{C}$  was  $1.29 \text{ keV} \pm 0.04 \text{ keV}$  at  $5.9 \text{ keV}$ ,  $1.32 \text{ keV} \pm 0.06 \text{ keV}$  at  $22.16 \text{ keV}$ ,  $1.34 \text{ keV} \pm 0.06 \text{ keV}$  at  $59.54 \text{ keV}$ , and  $1.43 \text{ keV} \pm 0.08 \text{ keV}$  at  $88.03 \text{ keV}$ . The results indicate that the detector did not suffer from incomplete charge collection, and that the spectrometer had better energy resolution at  $100^\circ\text{C}$  than any other multi-pixel radiation spectrometer so far reported.

## 1. Introduction

$\text{In}_{0.5}\text{Ga}_{0.5}\text{P}$  has only recently emerged as a suitable material for photon counting X-ray spectroscopy. Photodiodes made from this wide bandgap semiconductor material have been shown to be capable of spectroscopic response at room temperature [1] and above [2]. Single pixel  $\text{In}_{0.5}\text{Ga}_{0.5}\text{P}$  X-ray detectors have been reported with energy resolutions (Full Width at Half Maximum, FWHM) at  $5.9 \text{ keV}$  of  $770 \text{ eV}$  and  $1.27 \text{ keV}$  at  $20^\circ\text{C}$  and  $100^\circ\text{C}$ , respectively [2]. Due to the low leakage currents of such photodiode detectors, e.g.  $1.5 \text{ pA}$  at  $100^\circ\text{C}$  and an applied reverse bias of  $10 \text{ V}$ , including the leakage current contribution of the package [2] (a consequence of its  $1.9 \text{ eV}$  bandgap at room temperature [3–5] and the high quality of the epitaxial material), they can operate without cooling at high temperatures ( $\geq 20^\circ\text{C}$ ). Thus, radiation spectrometers with  $\text{In}_{0.5}\text{Ga}_{0.5}\text{P}$  detectors may be made with lower mass, volume, and power requirements than similar instruments based on conventional Si detector technologies which require cooling to limit thermally generated leakage currents [6,7]. Such uncooled high temperature operation is important for all applications which require miniature instrumentation with low power requirements. Benefits are likely to be found in space science where the impetus to develop such instrumentation is felt particularly keenly.

Importantly, the development of  $\text{In}_{0.5}\text{Ga}_{0.5}\text{P}$  X-ray and  $\gamma$ -ray detectors is aided by the fact that  $\text{In}_{0.5}\text{Ga}_{0.5}\text{P}$  structures can be grown nearly lattice matched with commercial GaAs substrates. Furthermore,

$\text{In}_{0.5}\text{Ga}_{0.5}\text{P}$  has higher X-ray absorption coefficients (e.g.  $15 \text{ cm}^{-1}$  at  $60 \text{ keV}$  [8,9]), compared to Si ( $0.3 \text{ cm}^{-1}$ ), SiC ( $0.3 \text{ cm}^{-1}$ ), GaAs ( $10 \text{ cm}^{-1}$ ), and AlInP ( $12 \text{ cm}^{-1}$ ) [8,9], which results in greater quantum detection efficiency per unit thickness.

Other wide bandgap technologies under development for spectroscopic X-ray and  $\gamma$ -ray detector arrays include GaAs [10–12], AlGaAs [13], and SiC [14]; Table 1 summarises the most important findings of these previous reports.

In this paper, a monolithic  $\text{In}_{0.5}\text{Ga}_{0.5}\text{P}$   $2 \times 2$  pixel array of square mesa photodiodes has been fabricated and characterised for the first time. The spectroscopic response of each pixel, up to an applied reverse bias of  $\leq 15 \text{ V}$ , was studied under the illumination of a  $154 \text{ MBq}$   $^{55}\text{Fe}$  radioisotope X-ray source, a  $298 \text{ MBq}$   $^{241}\text{Am}$  radioisotope X-ray and  $\gamma$ -ray source, and a  $246 \text{ MBq}$   $^{109}\text{Cd}$  radioisotope X-ray and  $\gamma$ -ray source using low-noise preamplifier electronics; all pixels were investigated at  $20^\circ\text{C}$  and one representative pixel was further studied up to  $100^\circ\text{C}$ . The maximum investigated applied reverse bias ( $= 15 \text{ V}$ ) exceeded the normal operating conditions of the spectrometer ( $= 5 \text{ V}$ ), which ensured maximum quantum detection efficiency, best energy resolution, and good charge transport.

This work demonstrates that small  $\text{In}_{0.5}\text{Ga}_{0.5}\text{P}$  detector arrays can now be produced, and furthermore, it shows the first results from any

\* Corresponding author.

E-mail address: [G.Lioliou@sussex.ac.uk](mailto:G.Lioliou@sussex.ac.uk) (G. Lioliou).

**Table 1**  
Previous reports on spectroscopic X-ray and  $\gamma$ -ray detector arrays.

Detector material	Array size	Pixel size ( $\mu\text{m}^2$ )	FWHM (keV)	Temperature ( $^\circ\text{C}$ )	Ref.
GaAs	$5 \times 5$	$200 \times 200$	0.270 @ 5.9	Room temp.	[10]
GaAs	$32 \times 32$	$350 \times 350$	0.300 @ 5.9	Room temp.	[11]
GaAs	$2 \times 2$	$200 \times 200$	$1.61 \pm 0.04$ @ 5.9	100	[12]
GaAs	$2 \times 2$	$200 \times 200$	$0.65 \pm 0.02$ @ 5.9	20	[12]
$\text{Al}_{0.2}\text{Ga}_{0.8}\text{As}$	$2 \times 2$	$200 \times 200$	0.76 @ 5.9	20	[13]
SiC	$2 \times 2$ ( $1 \times 3$ )	$250 \times 250$	1.36 @ 17.4	30	[14]

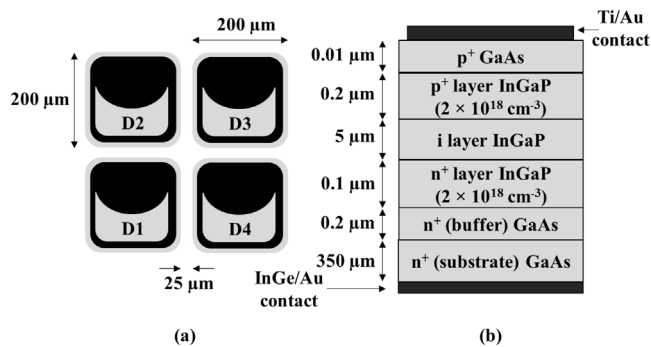


**Fig. 1.** (a) The layout of the  $\text{In}_{0.5}\text{Ga}_{0.5}\text{P}$   $2 \times 2$  square pixel photodiode array (not in scale) and (b) the layer structure of each  $\text{In}_{0.5}\text{Ga}_{0.5}\text{P}$  pixel (not in scale). The area covered by the top Ohmic contact is shown as the shaded area in (a); the device identification number (D1–D4) is shown in the schematic but did not appear on the devices themselves.

type of  $\text{In}_{0.5}\text{Ga}_{0.5}\text{P}$  radiation detector in response to high energy photons ( $> 21.17$  keV) up to 88.03 keV. An unprecedented energy resolution, for any X-ray detector array at  $100^\circ\text{C}$ , is achieved.

## 2. Array structure

Low-pressure (150 Torr) metalorganic vapour phase epitaxy (MOVPE) was used to grow an  $\text{In}_{0.5}\text{Ga}_{0.5}\text{P}$   $p^+i-n^+$  epilayer structure on an  $n^+$  GaAs substrate. The orientation of the epitaxial surface was  $\langle 100 \rangle$  with a miscut angle of  $10^\circ$  towards  $\langle 111 \rangle$ . The layer details are summarised in Table 2. The  $\text{In}_{0.5}\text{Ga}_{0.5}\text{P}$   $i$  layer was  $5 \mu\text{m}$  thick. A  $p^+$  GaAs layer was grown on top of the  $p^+$   $\text{In}_{0.5}\text{Ga}_{0.5}\text{P}$  layer to facilitate formation of a good Ohmic top contact. Ti/Au (20 nm/200 nm) were used for the top Ohmic contact (covering 50% of each pixel surface); InGe/Au (20 nm/200 nm) were used for the planar, common, bottom Ohmic contact. An array of four square mesa pixels was wet etched using a 1:1:1  $\text{K}_2\text{Cr}_2\text{O}_7:\text{HBr}:\text{CH}_3\text{COOH}$  solution followed by 10 s in a 1:8:80  $\text{H}_2\text{SO}_4:\text{H}_2\text{O}_2:\text{H}_2\text{O}$  finishing etch solution. A schematic diagram of the array is shown in Fig. 1. Each pixel was  $200 \mu\text{m} \times 200 \mu\text{m}$ , with a separation between adjacent pixels of  $25 \mu\text{m}$ . There was a  $10 \mu\text{m}$  radius at the corners of each pixel to protect against corner breakdown. The  $\text{In}_{0.5}\text{Ga}_{0.5}\text{P}$  array was packaged in a TO-5 can.

## 3. Electrical characterisation

The dark current and capacitance of each pixel, as a function of applied reverse bias and temperature, were measured. This work was performed in order for the electrical properties of the detector array to be investigated since they affect the performance of the photon counting spectrometer.

### 3.1. Dark current measurements

The dark current of each pixel as a function of applied reverse bias at temperatures from  $100^\circ\text{C}$  to  $20^\circ\text{C}$  (in  $20^\circ\text{C}$  steps) was measured using a Keysight B2981 A Femto/Picoammeter whilst the reverse bias up to 15 V (in 1 V steps) was applied using a Keithley

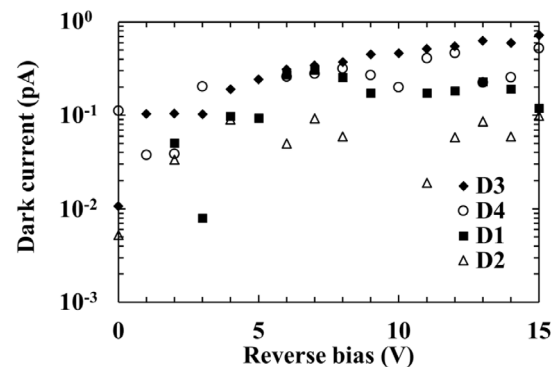


**Fig. 2.** Dark current of all pixels as a function of applied reverse bias at  $20^\circ\text{C}$ ; D1 (■), D2 ( $\Delta$ ), D3 ( $\blacklozenge$ ), and D4 ( $\circ$ ). The error bars ( $\leq 0.008$  pA) were smaller than the symbols.

2636B Source Measure Unit. A TAS Micro MT climatic cabinet was used for temperature control; dry  $\text{N}_2$  was constantly flowing inside the climatic cabinet thus maintaining an atmosphere with a relative humidity  $< 5\%$ . The uncertainty of the dark current measurements was calculated taking into account the inherent uncertainty of the Femto/Picoammeter and the uncertainty associated with repeatability (e.g. variations within a set of repeatable conditions of measurements). To establish the contribution of the TO-5 package to the measured dark currents, the leakage current of the package itself between each of the three empty pins (i.e. pins with no diode connected) and the common pin of the TO-5 package was measured.

The leakage current as a function of applied reverse bias of the four packaged pixels at  $20^\circ\text{C}$  is presented in Fig. 2; the leakage current varied from  $0.739 \text{ pA} \pm 0.008 \text{ pA}$  (D3) to  $0.098 \text{ pA} \pm 0.001 \text{ pA}$  (D2), at 15 V reverse bias, with a mean of  $0.4 \text{ pA} \pm 0.3 \text{ pA}$  (rms error). The leakage current of the package was  $0.4 \text{ pA} \pm 0.1 \text{ pA}$  (rms error) at  $20^\circ\text{C}$ , when 15 V potential difference was applied. This suggested that the leakage current of the package was the main contributor to the total leakage current of the pixels at  $20^\circ\text{C}$ , and that the variation of the leakage current of the packaged pixels arose from the variations of the leakage current of the package. The leakage current of the package arose from the epoxy, which insulated the non-common pins from the case, as well as leakage over the surface of the package.

The measured current of the packaged pixel D1 (i.e. including the package's leakage) as a function of applied reverse bias at different temperatures can be seen in Fig. 3; similar results were obtained for the other three pixels. The dark current of D1 decreased from  $3.05 \text{ pA} \pm 0.02 \text{ pA}$  at  $100^\circ\text{C}$  to  $0.119 \text{ pA} \pm 0.001 \text{ pA}$  at  $20^\circ\text{C}$ , at 15 V reverse bias, due to the reduced available thermal energy with decreasing temperature. The mean leakage current of all four packaged pixels at 15 V applied reverse bias at  $100^\circ\text{C}$  was  $2.7 \text{ pA} \pm 0.7 \text{ pA}$  (rms error). The leakage current of the package at 15 V applied potential different, at  $100^\circ\text{C}$ , was  $3.7 \text{ pA} \pm 0.6 \text{ pA}$  (rms error), suggesting that the leakage current of the package was, again, the main contributor to the total leakage current of the pixels at  $100^\circ\text{C}$ , similarly to the total leakage current of the pixels at  $20^\circ\text{C}$ . Assuming the pixels had the intended epilayer thicknesses and that the  $i$  layer was fully depleted at 15 V (see Section 3.2), the electric field strength resultant from the applied

**Table 2**  
Layer details of the  $\text{In}_{0.5}\text{Ga}_{0.5}\text{P}$  structure.

Layer	Material	Thickness ( $\mu\text{m}$ )	Dopant	Dopant type	Doping density ( $\text{cm}^{-3}$ )
1	GaAs	0.01	Zn	$\text{p}^+$	$1 \times 10^{19}$
2	InGaP	0.2	Zn	$\text{p}^+$	$2 \times 10^{18}$
3	InGaP	5	–	i	Nominally undoped
4	InGaP	0.1	Si	$\text{n}^+$	$2 \times 10^{18}$
5	GaAs	0.2	Si	$\text{n}^+$ (buffer)	$2 \times 10^{18}$
6	GaAs	350	Si	$\text{n}^+$ (substrate)	$2 \times 10^{18}$

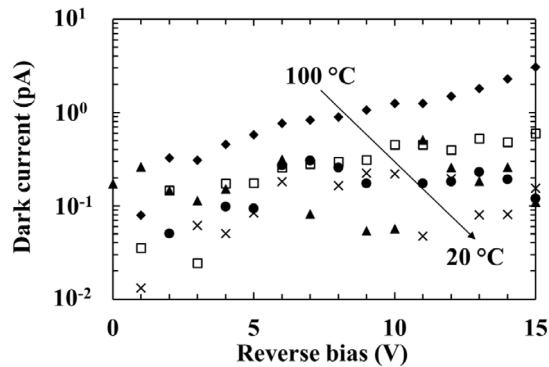


**Fig. 3.** Dark current of D1 as a function of reverse bias at 100 °C ( $\blacklozenge$ ), 80 °C ( $\square$ ), 60 °C ( $\times$ ), 40 °C ( $\blacktriangle$ ), and 20 °C ( $\circ$ ). The error bars ( $\leq 0.02$  pA) were smaller than the symbols.

bias was  $30 \text{ kV cm}^{-1}$ . Hence, it was concluded that at temperatures  $\leq 100$  °C and applied electric field strengths  $\leq 30 \text{ kV cm}^{-1}$ , the leakage current of the pixels was insignificant; the leakage current of the package dominated the total leakage current. These results show that semiconductor device technology for high temperature spectrometry applications has advanced beyond the capabilities of the packaging technology of traditionally TO type cans. The development of custom high temperature tolerant low noise semiconductor packaging is likely required for optimal performance of emerging high temperature tolerant radiation detectors based on InGaP and similar materials.

### 3.2. Capacitance measurements

The capacitances of the four pixels were measured in dark conditions at temperatures from 100 °C to 20 °C (in 20 °C steps) using an HP 4275 A Multi Frequency LCR meter; the reverse bias (up to 15 V, in 1 V steps) was applied using a Keithley 6487 Picoammeter/Voltage Source. The test signal of the LCR meter was sinusoidal with a frequency of 1 MHz and a magnitude of 50 mV rms. A frequency of 1 MHz was chosen to minimise the (complex) contributions of the deep level impurities and traps in the extraction of the effective carrier concentrations. The capacitance measurements allowed the calculation of the depletion layer width and the effective carrier concentration within the i layer of the pixels. A TAS Micro MT climatic cabinet, with dry  $\text{N}_2$  flowing inside of it, was used for temperature control. The uncertainty associated with the reported depletion layer capacitances for each pixel was estimated to be  $\pm 0.04$  pF, whereas the uncertainties for the reported capacitance variations with applied reverse bias and temperature (i.e. when no interconnections were changed within a single set of measurements taken at the same conditions) was proportional to the value of the corresponding measured capacitance, and it was estimated to be  $\pm 0.006$  pF. The capacitance between an empty pin (i.e. a pin with no diode connected) and the common pin of the TO-5 package was also measured and subtracted from the total measured capacitance of each pixel, thus resulting in the depletion layer capacitance.

The depletion layer capacitance of pixel D1 (with the packaging capacitance subtracted) as a function of applied reverse bias at 20 °C

can be seen in Fig. 4(a); similar results were obtained for the other three pixels. The capacitance of the four pixels varied from  $0.85 \text{ pF} \pm 0.04 \text{ pF}$  (D3) to  $0.89 \text{ pF} \pm 0.04 \text{ pF}$  (D2) at 15 V reverse bias at this temperature. The capacitance of D1 as a function of temperature at 0 V and 15 V applied reverse bias is reported in Fig. 4(b); similar dependences were found for the other three pixels. The depletion layer capacitance of D1 decreased from  $1.110 \text{ pF} \pm 0.006 \text{ pF}$  at 100 °C to  $1.020 \text{ pF} \pm 0.006 \text{ pF}$  at 20 °C when no reverse bias was applied, whereas it was temperature invariant ( $0.890 \text{ pF} \pm 0.006$  at 100 °C to  $0.883 \text{ pF} \pm 0.006$  at 20 °C) at 15 V applied reverse bias. The mean capacitance of the four pixels, at 15 V applied reverse bias and across the temperature range 100 °C to 20 °C, was  $0.88 \text{ pF} \pm 0.02 \text{ pF}$  (rms error).

The depletion layer width and the effective carrier concentration within the i layer were calculated from the capacitance measurements. The depletion layer width was estimated using the assumption of a parallel plate capacitance [15] and an  $\text{In}_{0.5}\text{Ga}_{0.5}\text{P}$  relative permittivity of 11.7 [16]; the calculated depletion layer width of D1 at 20 °C is shown in Fig. 5(a). It increased from  $4.08 \pm 0.02 \mu\text{m}$  at 0 V to  $4.65 \pm 0.03 \mu\text{m}$  at 5 V, whereas it remained constant at reverse biases  $\geq 5$  V, indicating that full depletion achieved at 5 V. Maximum depletion widths of  $4.9 \mu\text{m} \pm 0.3 \mu\text{m}$ ,  $4.7 \mu\text{m} \pm 0.3 \mu\text{m}$ ,  $4.7 \mu\text{m} \pm 0.3 \mu\text{m}$ , and  $4.8 \mu\text{m} \pm 0.3 \mu\text{m}$  were calculated for D1, D2, D3, and D4, respectively, at 20 °C. The Debye length ( $0.3 \mu\text{m}$  at 100 °C and  $0.2 \mu\text{m}$  at 20 °C) was considered in the calculation of the depletion layer width uncertainty; as can be seen from the stated uncertainties, the Debye length dominated the other uncertainties. Such values were compatible with measurements taken during epitaxial growth, which showed an i layer thickness of  $5 \mu\text{m}$ . The depletion layer width of D1 as a function of temperature at reverse biases of 0 V and 15 V is presented in Fig. 5(b); similar results were obtained for the other three pixels. The depletion width at low applied reverse biases was temperature dependent, increasing from  $3.74 \mu\text{m} \pm 0.02 \mu\text{m}$  at 100 °C to  $4.08 \mu\text{m} \pm 0.02 \mu\text{m}$  at 20 °C at no applied bias, whereas the depletion width at 15 V applied reverse bias was temperature invariant across the temperature range explored.

The carrier concentration of the i layer was calculated using the equation for general non-uniform distribution [15] and it is shown in Fig. 6 for D1 at 20 °C. Similar results were obtained for the other three pixels. An effective carrier concentration of  $3.7 \times 10^{14} \text{ cm}^{-3} \pm 0.4 \times 10^{14} \text{ cm}^{-3}$  was found within the i layer; this value increased to  $2 \times 10^{17} \text{ cm}^{-3}$ , with an uncertainty ( $\pm 16 \times 10^{17} \text{ cm}^{-3}$ ) larger than the value, at deeper distances, i.e. closer to the  $\text{i-n}^+$  interface.

## 4. Spectroscopic measurements, results, and discussions

X-ray and  $\gamma$ -ray spectra were accumulated with all four pixels to investigate their spectroscopic performance, compare the spectroscopic responses between them, and identify the limiting factors to the energy resolution achieved with the associated spectrometer. Each  $\text{In}_{0.5}\text{Ga}_{0.5}\text{P}$  pixel, in turn, was coupled to a low-noise charge-sensitive preamplifier. The custom-made charge-sensitive preamplifier was of a feedback resistorless design, similar to Ref. [17], with a noise, when unloaded, of  $\approx 40 \text{ e}^-$  rms at 20 °C. The array-preamplifier system was installed inside a TAS Micro LT climatic cabinet for temperature control. The relative humidity of the atmosphere inside the chamber was  $< 5\%$  (achieved through a continuous flow of dry  $\text{N}_2$ ). The preamplifier output was shaped by an ORTEC 572 A shaping amplifier with selectable shaping

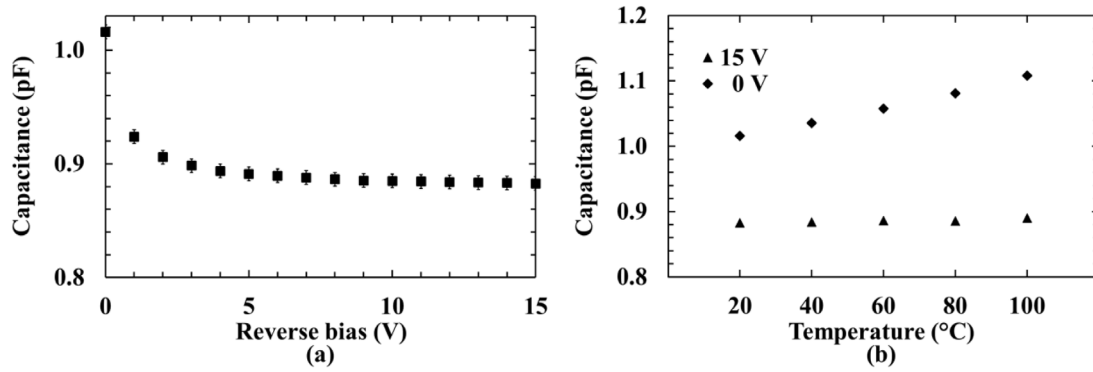


Fig. 4. Capacitance (a) as a function of reverse bias of pixel D1 (■) at 20 °C (similar capacitances, within uncertainties, were measured for the rest of the pixels) and (b) as a function of temperature of D1 at 0 V (◆) and 15 V (▲) reverse bias. The error bars ( $\pm 0.006$  pF) were smaller than the symbols in (b).

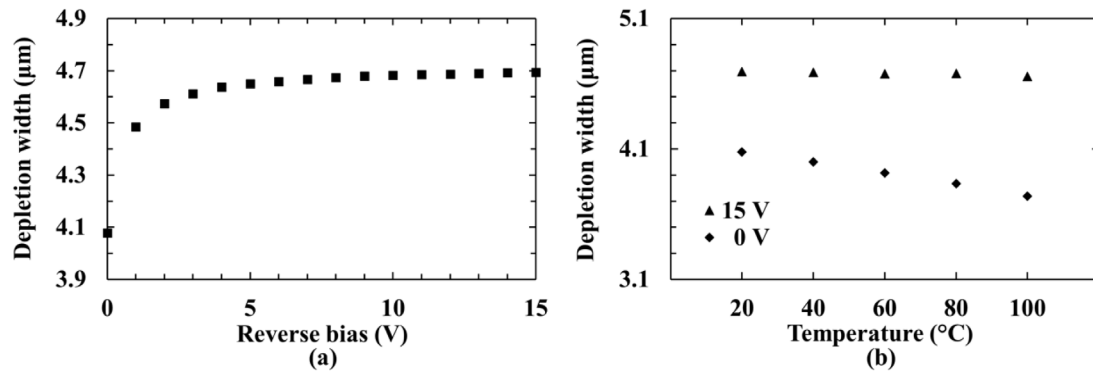


Fig. 5. Depletion width (a) as a function of reverse bias for D1 (■) at 20 °C (similar depletion widths, within uncertainties, were calculated for the rest of the pixels) and (b) as a function of temperature for D1 at 0 V (◆) and 15 V (▲) reverse bias. The error bars ( $\leq 0.03$  μm) were smaller than the symbols.

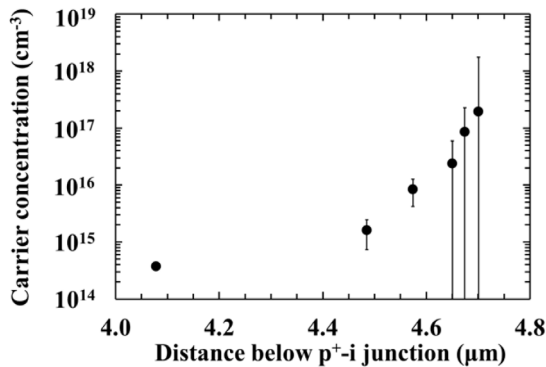


Fig. 6. Calculated carrier concentration in the i layer of D1 as a function of distance below the p<sup>+</sup>-i junction at 20 °C.

times of 0.5 μs, 1 μs, 2 μs, 3 μs, 6 μs, and 10 μs. An ORTEC EASY-MCA-8K multichannel analyser (MCA) was then used to digitise the signal from the output of the shaping amplifier. Three radioisotope sources were used: <sup>55</sup>Fe, emitting X-rays; <sup>241</sup>Am, emitting X-rays and γ-rays; and <sup>109</sup>Cd, emitting X-rays and γ-rays.

#### 4.1. <sup>55</sup>Fe radioisotope X-ray source

A 154 MBq <sup>55</sup>Fe X-ray radioisotope source, with characteristic emissions of Mn K $\alpha$  (5.9 keV) and Mn K $\beta$  (6.49 keV) X-rays was placed  $\approx 3$  mm above the top of the array. It was encapsulated in a stainless steel capsule with a 250 μm thick Be X-ray window. <sup>55</sup>Fe X-ray spectra were accumulated initially with all four pixels at 20 °C. Following this, spectra were accumulated with D1, while the array-preamplifier system

was operated at temperatures from 100 °C to 20 °C, in 20 °C steps. At each temperature and for each pixel, spectra were accumulated as a function of applied reverse bias (0 V, 5 V, 10 V, and 15 V) and shaping time (0.5 μs, 1 μs, 2 μs, 3 μs, 6 μs, and 10 μs). The live time limit of each spectrum was 120 s.

An <sup>55</sup>Fe X-ray spectrum accumulated using D1, at 2 μs shaping time and 5 V reverse bias, can be seen in Fig. 7. The main detected photopeak was the combination of the Mn K $\alpha$  and Mn K $\beta$  peaks, from the detection of the X-rays emitted from the <sup>55</sup>Fe radioisotope X-ray source. The main photopeak was deconvolved into the respective Mn K $\alpha$  and Mn K $\beta$  contributions by fitting Gaussians representing the characteristic emissions to the main detected photopeak. The relative emission ratio of the <sup>55</sup>Fe radioisotope X-ray source at 6.49 keV and 5.9 keV (= 0.14 [18]), the attenuation through the Be window, and the relative quantum detection efficiency of the pixels at those energies were all taken into account. The energy calibration of the MCA charge scale of each spectrum was achieved using the position (centroid channel number) of the zero energy noise peak and the fitted Mn K $\alpha$  peak. The FWHM at 5.9 keV (Mn K $\alpha$ ) was recorded for all spectra. The low energy tail, shown in the spectrum of Fig. 7, was attributed to the partial collection of charge created in non-active layers [19]. The valley to peak (V/P) ratio, defined as the ratio between the number of counts at the channel corresponding to 3.5 keV and at the centroid channel of the fitted peak at 5.9 keV (Mn K $\alpha$ ) was calculated to be 0.03 for the spectrum shown in Fig. 7; this value was comparable to that reported for GaAs square pixels (0.02 to 0.09 at 20 °C [12]).

The best (narrowest) FWHM at 5.9 keV was achieved at 2 μs shaping time, and it improved when the reverse bias was increased from 0 V to 5 V; at reverse biases  $\geq 5$  V, the FWHM remained constant within uncertainties. The energy resolution (FWHM at 5.9 keV) achieved with three of the pixels was the same (750 eV  $\pm$  30 eV with D1 and D4; 760 eV  $\pm$  30 eV with D2), whereas 810 eV  $\pm$  30 eV FWHM at 5.9

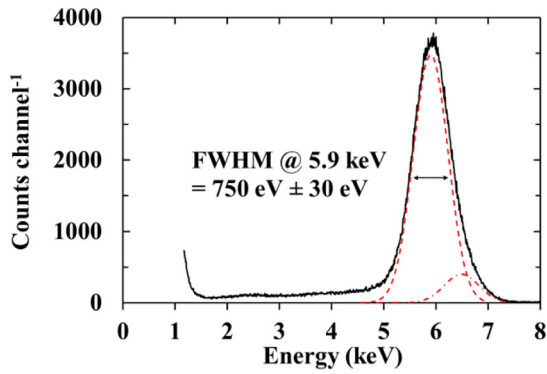


Fig. 7.  $^{55}\text{Fe}$  X-ray spectrum accumulated with pixel D1 and the spectrometer electronics (5 V applied reverse bias; 2  $\mu\text{s}$  shaping time) at 20  $^{\circ}\text{C}$ .

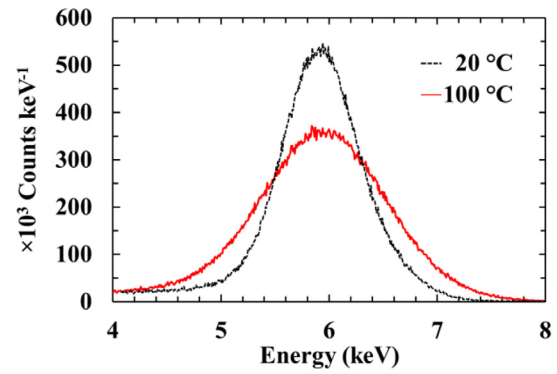


Fig. 9. Comparison between the  $^{55}\text{Fe}$  X-ray spectra accumulated with the D1 at 100  $^{\circ}\text{C}$  (5 V reverse bias and 1  $\mu\text{s}$  shaping time; FWHM at 5.9 keV = 1.29 keV  $\pm$  0.04 keV; —) and at 20  $^{\circ}\text{C}$  (5 V reverse bias and 2  $\mu\text{s}$  shaping time; FWHM at 5.9 keV = 0.78 keV  $\pm$  0.03 keV; - - -).

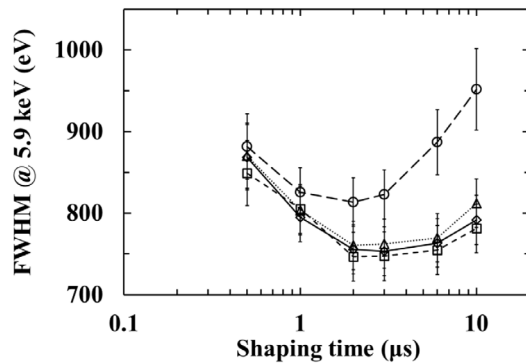


Fig. 8. FWHM at 5.9 keV (Mn  $K\alpha$ ) as a function of shaping time at a reverse bias of 5 V and a temperature of 20  $^{\circ}\text{C}$  with pixels D1 ( $\diamond$ ), D2 ( $\triangle$ ), D3 ( $\circ$ ), and D4 ( $\square$ ). Lines (— for D1,  $\cdots$  for D2, — — for D3, and - - - for D4) are guides for the eyes only.

keV was achieved with D3, at 5 V and 2  $\mu\text{s}$ . The mean FWHM at 5.9 keV at 20  $^{\circ}\text{C}$  of all pixels was 770 eV  $\pm$  30 eV (rms error). Slightly broader FWHM at 5.9 keV was obtained at 0 V applied reverse bias cf. that at 5 V; it varied between 810 eV  $\pm$  30 eV and 850 eV  $\pm$  30 eV among the four pixels, using a shaping time of 2  $\mu\text{s}$ . The improvement of the energy resolution at increased applied reverse biases is discussed below. A summary of the FWHM at 5.9 keV achieved with each pixel as a function of shaping time at 5 V applied reverse bias is shown in Fig. 8.

The best FWHM at 5.9 keV was similar to that achieved using a single pixel circular mesa  $\text{In}_{0.5}\text{Ga}_{0.5}\text{P}$  X-ray photodiode (770 eV FWHM at 5.9 keV at 20  $^{\circ}\text{C}$ ) [1]. The results reported here are also comparable to those achieved with  $\text{Al}_{0.2}\text{Ga}_{0.8}\text{As}$  pixel arrays (760 eV at 5.9 keV [13]), but not as good as those achieved with a GaAs array (650 eV  $\pm$  20 eV at 5.9 keV [12]); all were operated at a temperature of 20  $^{\circ}\text{C}$  and used similar preamplifier electronics. Given the different electron-hole pair creation energies at 20  $^{\circ}\text{C}$  of these three materials (4.94 eV for  $\text{In}_{0.5}\text{Ga}_{0.5}\text{P}$  [2], 4.43 eV for  $\text{Al}_{0.2}\text{Ga}_{0.8}\text{As}$  [20], and 4.184 eV for GaAs [21]), different Equivalent Noise Charges (ENC) were indicated; 64  $e^-$  rms for  $\text{In}_{0.5}\text{Ga}_{0.5}\text{P}$ , 74  $e^-$  rms for  $\text{Al}_{0.2}\text{Ga}_{0.8}\text{As}$ , and 66  $e^-$  rms for GaAs arrays. Better energy resolutions (270 eV [10] and 300 eV [11] FWHM at 5.9 keV) have been reported for larger GaAs arrays at a similar temperature in the past, but those results have not been replicated directly by other groups and also used substantially lower-noise readout electronics — optimisation of the connection between detector and input JFET played a key role [10,11,22].

The spectroscopic response of a representative pixel, D1, was then further investigated at temperatures from 100  $^{\circ}\text{C}$  to 20  $^{\circ}\text{C}$ , in 20  $^{\circ}\text{C}$  steps. The FWHM at 5.9 keV improved as the applied reverse bias increased from 0 V to 5 V, at all temperatures. The FWHM at 5.9 keV

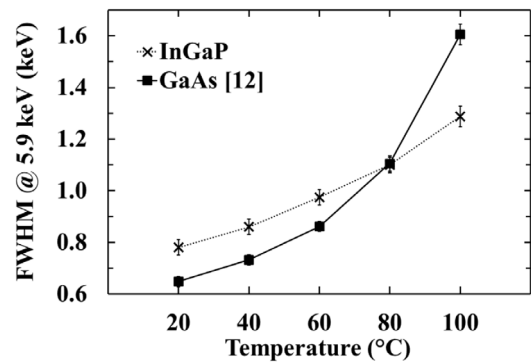


Fig. 10. The best FWHM at 5.9 keV achieved with D1 ( $\times$ ) across the temperature range investigated. For comparison, the FWHM at 5.9 keV for a comparable GaAs array spectrometer ( $\blacksquare$ ) is also shown [12]. Lines ( $\cdots$  for InGaP and — for GaAs) are guides for the eyes only.

at 5 V improved with reducing temperature, from 1.29 keV  $\pm$  0.04 keV (109  $e^-$  rms ENC) at 100  $^{\circ}\text{C}$  (1  $\mu\text{s}$  shaping time) to 0.78 keV  $\pm$  0.03 keV (67  $e^-$  rms ENC) at 20  $^{\circ}\text{C}$  (2  $\mu\text{s}$  shaping time). A comparison of the spectra accumulated at 100  $^{\circ}\text{C}$  and 20  $^{\circ}\text{C}$  at the shaping times that gave the best energy resolution (narrowest FWHM at 5.9 keV) can be seen in Fig. 9. It should be noted that the number of counts  $\text{keV}^{-1}$  is reported in each case to allow the comparison between the spectra. This was necessary since the MCA channel width (in terms of eV) differed at different temperatures and shaping times as a consequence of the preamplifier change in the conversion factor.

The best FWHM at 5.9 keV at each investigated temperature is presented in Fig. 10. A shaping time of 1  $\mu\text{s}$  was best at temperatures  $>$  60  $^{\circ}\text{C}$  and a shaping time of 2  $\mu\text{s}$  was best at temperatures  $\leq$  60  $^{\circ}\text{C}$ . However, considering the uncertainties of the FWHM associated with the Gaussian fitting, the best FWHM at 5.9 keV was achieved between 0.5  $\mu\text{s}$  and 3  $\mu\text{s}$  at temperatures  $\geq$  60  $^{\circ}\text{C}$  and between 1  $\mu\text{s}$  and 6  $\mu\text{s}$  at temperatures  $<$  60  $^{\circ}\text{C}$ . The best energy resolution (FWHM at 5.9 keV) achieved with a previously reported GaAs pixel array [12] is also included in Fig. 10 for comparison. At 100  $^{\circ}\text{C}$ , the energy resolution achieved using D1 was similar to that reported using an earlier  $\text{In}_{0.5}\text{Ga}_{0.5}\text{P}$  single pixel circular mesa photodiode (FWHM at 5.9 keV of 1.27 keV, 107  $e^-$  rms ENC) [2]. D1 had better energy resolution at 100  $^{\circ}\text{C}$  than has been reported with a GaAs pixel array (FWHM at 5.9 keV of 1.61  $\pm$  0.04 keV at 100  $^{\circ}\text{C}$ , 166  $e^-$  rms  $\pm$  4  $e^-$  rms ENC) [12], which used similar preamplifier electronics.

The dependency of the FWHM at 5.9 keV on shaping time, at all investigated temperatures, can be seen in Fig. 11. The FWHM at 5.9 keV improved as the shaping time lengthen from 0.5  $\mu\text{s}$  to the optimum

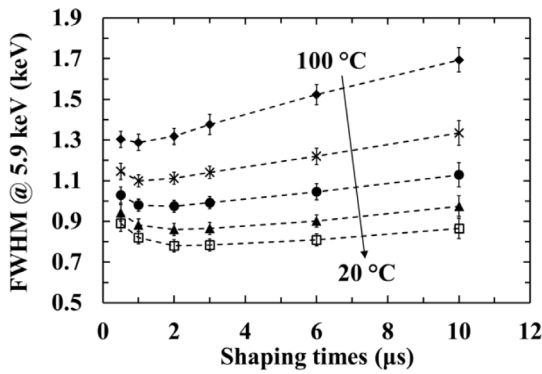


Fig. 11. FWHM at 5.9 keV achieved with D1 at 5 V applied reverse bias as a function of shaping time at 100 °C (◆), at 80 °C (×), at 60 °C (★), at 40 °C (▲), and at 20 °C (□). Lines (---) are guides for the eyes only.

shaping time (see below) and then deteriorate for further lengthening of the shaping time. The effect of the temperature on the FWHM at 5.9 keV is also shown in Fig. 11. These observations are discussed in the following paragraphs, along with the noise analysis of the spectroscopic system.

Fano noise, incomplete charge collection noise, and electronic noise all degrade the spectral resolution of a non-avalanche semiconductor photodiode detector based spectrometer. The Fano noise is related to the statistical nature of the charge creation process; it is proportional to the electron-hole pair creation energy, the Fano factor, and the energy of the absorbed photon [23]. Considering the experimentally measured electron-hole pair creation energy values of 5.02 eV at 100 °C and 4.94 eV at 20 °C [2], and a Fano factor of 0.13 [24], the Fano noise of  $\text{In}_{0.5}\text{Ga}_{0.5}\text{P}$  at 5.9 keV was calculated to be 146 eV at 100 °C and 145 eV at 20 °C. It should be noted that the Fano factor is likely to be dependent on temperature, but its temperature dependence has not yet been reported for  $\text{In}_{0.5}\text{Ga}_{0.5}\text{P}$ . The incomplete charge collection noise is the result of carrier trapping and recombination processes [25]. The electronic noise consists of parallel white noise, series white noise (including induced gate current noise),  $1/f$  noise, and dielectric noise [26,27]. The  $1/f$  (flicker) noise results from the fluctuation of the drain current of the preamplifier input transistor (JFET in the present case) due to the generation/recombination of carriers in the two depleted regions of the transistor from impurities and defects; an infinite number of uniformly distributed time constants of such events (generation/recombination) is assumed [26].

The leakage current of the pixel (including its package contribution), and the preamplifier input JFET give rise to the parallel white noise; whilst the capacitance of the pixel (including its packaging contribution), the preamplifier input JFET, the feedback capacitance,

the test capacitance (if present), and the stray capacitances acting at the gate of the JFET give rise to the series white noise and to the  $1/f$  noise [26–28]. Lossy dielectrics in close proximity to the input of the preamplifier, such as the feedback capacitance, the input JFET dielectrics, passivation, and packaging, and the pixel and its packaging, give rise to the dielectric noise. The parallel white noise and the series white noise are, respectively, proportional and inversely proportional to the shaping time; the Fano noise, the incomplete charge collection noise, the  $1/f$  noise, and the dielectric noise are instead shaping time invariant [26,27]. The best energy resolution (minimum ENC) occurs at the optimum shaping time, where the quadratic sum of the white series and the white parallel noise is minimised, i.e. where the white series noise and the white parallel noise are equal. Depending on the corresponding white series and white parallel noise contributions, the optimum shaping time may differ at each temperature. It should be noted that the optimum available shaping time may be different from the optimum shaping time if the available shaping amplifier cannot be infinitely continuously (cf. discretely) adjusted.

A multidimensional least squares technique was used to fit the experimental values of the FWHM at 5.9 keV as a function of shaping time (shown in Fig. 11) to detangle the different noise contributions. The multidimensional least squares fitting of the experimental FWHM at 5.9 keV achieved with D1 (at 5 V applied reverse bias) at 100 °C and at 20 °C is presented in Fig. 12. The white parallel (WP), the white series (WS), and the shaping time,  $\tau$ , invariant (quadratic sum of the Fano noise, the incomplete charge collection noise, the  $1/f$  noise, and the dielectric noise) noise contributions were determined. Fig. 12 suggested that the  $\tau$  invariant noise was the dominant source of noise within the investigated shaping time range at both temperatures. The white series noise and the white parallel noise were equal at 1 μs at 100 °C and between 2 μs and 3 μs at 20 °C; these were the optimum shaping time at each temperature. The reduction of the WP noise contribution, due to the reduction of the total leakage current of the spectroscopic system as the temperature reduced from 100 °C to 20 °C (shown in Fig. 12), resulted in the observed lengthening of the optimum shaping time for the same temperature reduction. Subtracting in quadrature the calculated Fano noise and the  $1/f$  noise from the  $\tau$  invariant noise, the residual noise was calculated at each temperature; the residual noise was the combined contribution of the incomplete charge collection noise (if present) and the dielectric noise. It should be noted that the contribution of the incomplete charge collection noise at 5 V was found to be negligible, as discussed in Section 4.4; therefore, the residual noise consisted only of dielectric noise and was the main noise contribution to the reported  $\text{In}_{0.5}\text{Ga}_{0.5}\text{P}$  spectrometer.

The extracted total dielectric noise for pixel D1 used in the spectrometer within the investigated temperature range is presented in Fig. 13; it decreased from 100 e<sup>-</sup> rms ENC at 100 °C to 59 e<sup>-</sup> rms ENC at 20 °C. The combined dielectric noise contribution of the pixel and the input JFET themselves (i.e. excluding the contribution of

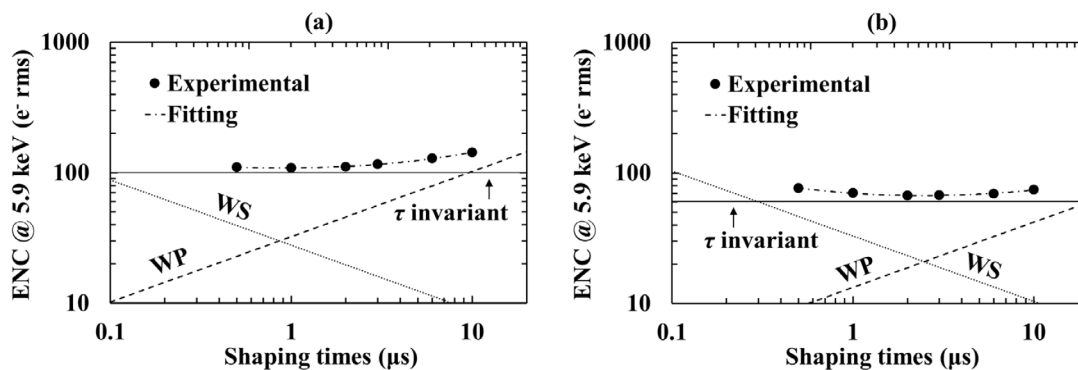


Fig. 12. Noise components present in the spectrometer at 5.9 keV at temperatures of (a) 100 °C and (b) 20 °C. A multidimensional least square fitting to the experimental points was used to determine the white parallel (WP), the white series (WS), and the shaping time invariant (combination of the Fano noise,  $1/f$  noise, and residual noise) noise contributions.

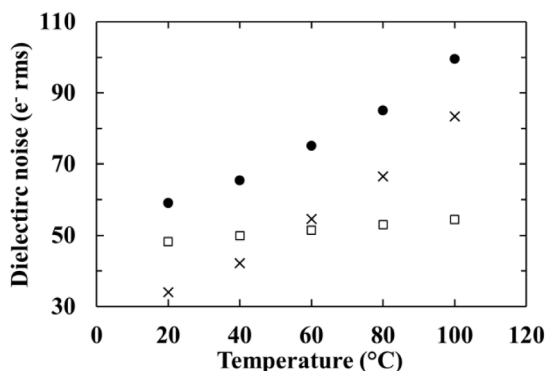


Fig. 13. Total dielectric noise (●) as a function of temperature, at 5 V. The readily calculated dielectric noise (arising from D1 and the input JFET) (□), as well as the remaining dielectric noise (arising from the feedback capacitance, the passivation and packaging of both the input JFET and the pixel, and any stray dielectrics in close proximity to the input of the preamplifier) (×) are also shown. The error bars ( $< 1 e^-$  rms) were smaller than the symbols.

their passivation and packaging) was calculated assuming a dissipation factor of  $6.5 \times 10^{-3}$  for  $\text{In}_{0.5}\text{Ga}_{0.5}\text{P}$  [1] and  $0.2 \times 10^{-3}$  for Si [29]. It was found to reduce from  $54 e^-$  rms ENC at  $100^\circ\text{C}$  to  $48 e^-$  rms ENC at  $20^\circ\text{C}$ . The remaining quantity of the dielectric noise (arising from all the lossy dielectrics in close proximity to the input of the preamplifier, including the feedback capacitance, the passivation and packaging of both the input JFET and the pixel [22,27,30], and any stray dielectrics) reduced from  $83 e^-$  rms ENC at  $100^\circ\text{C}$  to  $34 e^-$  rms ENC at  $20^\circ\text{C}$ . This remainder dominated the total noise for temperatures  $\geq 60^\circ\text{C}$ , whereas the dielectric noise of the pixel dominated at  $40^\circ\text{C}$  and  $20^\circ\text{C}$ .

The observed improvement of the energy resolution with an increased applied reverse bias, from 0 V to 5 V, was attributed to the reduction of both the white series noise (due to the reduction of the capacitance of each pixel, see Fig. 4) and the incomplete charge collection noise (due to the improvement in the charge collection efficiency at the increased internal electric field strength). Given that the capacitance of each pixel did not further reduce for an applied reverse bias increase beyond 5 V (Fig. 4), any change in the energy resolution for a reverse bias increase  $> 5$  V would be attributed to the changes in the parallel white noise and/or incomplete charge collection noise. However, the change of both of these noise contributions as the reverse bias was increased from 5 V to 15 V was insignificant; the energy resolution (FWHM at 5.9 keV) remained stable. Thus it appears there was no incomplete charge collection noise at 5.9 keV, for  $\geq 5$  V applied reverse bias. However, the incomplete charge collection noise is known to be photon energy dependent [11], and measurements with higher energy photons were required to explore the possibility of incomplete charge collection noise at higher energies; this is presented in Section 4.4.

#### 4.2. $^{241}\text{Am}$ radioisotope X-ray and $\gamma$ -ray source

X-ray and  $\gamma$ -ray spectra were then accumulated with an  $^{241}\text{Am}$  radioisotope X-ray and  $\gamma$ -ray source illuminating the pixel array, using the same experimental set up as the one for the  $^{55}\text{Fe}$  X-ray spectra. The  $^{241}\text{Am}$  radioisotope X-ray and  $\gamma$ -ray source had an activity of 298 MBq, and it was encapsulated in a stainless steel capsule with a 250  $\mu\text{m}$  thick Be window, which fully absorbed the associated  $^{241}\text{Am}$   $\alpha$  particles. Thus only the characteristic X-rays and  $\gamma$ -rays illuminated the array. Firstly, spectra were accumulated using all four  $\text{In}_{0.5}\text{Ga}_{0.5}\text{P}$  pixels at  $20^\circ\text{C}$ , in turn. The spectroscopic response of a pixel D1 was then investigated under the illumination of the  $^{241}\text{Am}$  radioisotope X-ray and  $\gamma$ -ray source as a function of temperature (from  $100^\circ\text{C}$  to  $20^\circ\text{C}$ , in  $20^\circ\text{C}$  steps). For each  $\text{In}_{0.5}\text{Ga}_{0.5}\text{P}$  pixel and at each temperature, only one spectrum was obtained at an applied reverse bias of 5 V and at the optimum available shaping time as was indicated by the results

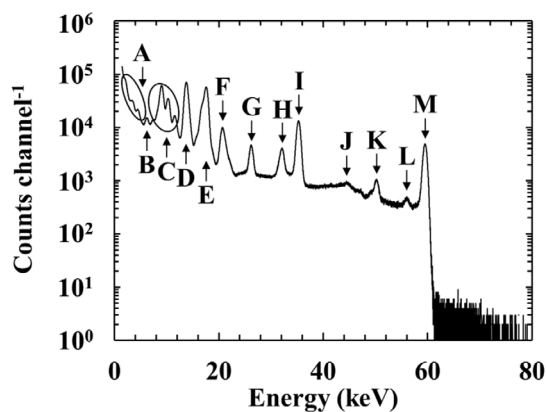


Fig. 14.  $^{241}\text{Am}$  X-ray and  $\gamma$ -ray spectrum accumulated with D1 at  $20^\circ\text{C}$  (5 V reverse bias and 2  $\mu\text{s}$  shaping time). Details of the major peaks identified can be found in Table 3. The counts beyond the 59.54 keV  $\gamma$ -ray peak (a total of  $\approx 2.6 \times 10^3$ , cf.  $4.6 \times 10^7$  in the rest of the spectrum) arise from pile-up.

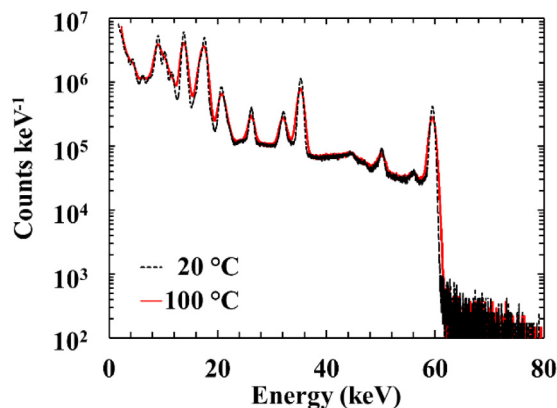


Fig. 15.  $^{241}\text{Am}$  X-ray and  $\gamma$ -ray spectra obtained with D1 at  $100^\circ\text{C}$  (5 V reverse bias and 1  $\mu\text{s}$  shaping time, —) and  $20^\circ\text{C}$  (5 V reverse bias and 2  $\mu\text{s}$  shaping time, - - -).

obtained with the  $^{55}\text{Fe}$  radioisotope X-ray source (see Section 4.1). The live time limit was set to 86400 s (24 h).

The accumulated  $^{241}\text{Am}$  X-ray and  $\gamma$ -ray spectrum using D1 at  $20^\circ\text{C}$  can be seen in Fig. 14; similar spectra were recorded for the other three pixels. The characteristic emissions of the  $^{241}\text{Am}$  X-ray and  $\gamma$ -ray source [31,32], the characteristic detector fluorescence peaks, the stainless-steel capsule fluorescence peak, and escape peaks, were all identified in Fig. 14. Details of the origin of each peak are presented in Table 3. The counts above 59.54 keV in the spectrum ( $\approx 2.6 \times 10^3$ , 0.006% of the total detected) were attributed to pulse pile-up. A Gaussian peak was fitted to the 59.54 keV  $\gamma$ -ray photopeak; the FWHM at 59.54 keV was  $850 \text{ eV} \pm 40 \text{ eV}$  for D1, D2, and D4, and  $910 \text{ eV} \pm 40 \text{ eV}$  for D3, at  $20^\circ\text{C}$ . The mean FWHM at 59.54 keV across all pixels was  $870 \text{ eV} \pm 30 \text{ eV}$  (rms error).

The  $^{241}\text{Am}$  X-ray and  $\gamma$ -ray spectra accumulated with D1 at  $100^\circ\text{C}$  and  $20^\circ\text{C}$  are presented in Fig. 15; to allow comparisons, the spectra were calibrated in terms of counts  $\text{keV}^{-1}$ , as above. Gaussians were fitted to the main photopeak, at the 59.54 keV  $\gamma$ -ray photopeak, and the associated FWHM was recorded as a function of temperature; this is shown in Fig. 16. The FWHM at 59.54 keV improved from  $1.34 \text{ keV} \pm 0.06 \text{ keV}$  at  $100^\circ\text{C}$  to  $0.86 \text{ keV} \pm 0.04 \text{ keV}$  at  $20^\circ\text{C}$ .

#### 4.3. $^{109}\text{Cd}$ radioisotope X-ray and $\gamma$ -ray source

X-ray and  $\gamma$ -ray spectra were then accumulated with a  $^{109}\text{Cd}$  radioisotope X-ray and  $\gamma$ -ray source illuminating the pixel array, using

**Table 3**

Origin of each peak identified in Fig. 14 ( $^{241}\text{Am}$  X-ray and  $\gamma$ -ray spectrum) [31] [32]. The type of each peak (characteristic emission from the source, CE; fluorescence peak, FP; escape peak, EP) is also shown for the convenience of the reader.

Peak label Fig. 14	Energy (keV)	Name	Type
A	2–4.7	Ga ( $K\alpha$ , $K\beta$ ) & As ( $K\alpha$ , $K\beta$ ) from Np $L\alpha$	EP
B	6.4	Fe $K\alpha$ (capsule)	FP
C	8.5	Ga ( $K\alpha$ ) from Np $L\beta$	EP
C	9.27–11.78	Ga ( $K\alpha$ , $K\beta$ ) & As ( $K\alpha$ , $K\beta$ ) from Np $L\gamma$	EP
C	9.2	Ga $K\alpha$ (detector)	FP
C	10.3	Ga $K\beta$ (detector)	FP
C	10.5	As $K\alpha$ (detector)	FP
C	11.7	As $K\beta$ (detector)	FP
D	13.76	Np $L\alpha_2$	CE
D	13.95	Np $L\alpha_1$	CE
E	16.11–17.99	Np $L\beta$	CE
F	20.78–21.49	Np $L\gamma$	CE
G	26.35	$\gamma$ -ray	CE
H	32.3	In ( $K\beta$ ) from 59.54 keV	EP
I	33.2	$\gamma$ -ray	CE
I	35.3	In ( $K\alpha$ ) from 59.54 keV	EP
J	43.4	$\gamma$ -ray	CE
K	47.8–50.3	Ga ( $K\alpha$ , $K\beta$ ) & As ( $K\alpha$ , $K\beta$ ) from 59.54 keV	EP
L	56.3	In ( $L\alpha$ ) from 59.54 keV	EP
M	59.54	$\gamma$ -ray	CE

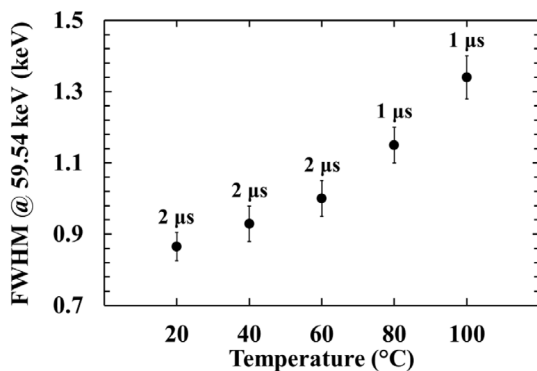


Fig. 16. FWHM at 59.54 keV achieved with D1 as a function of temperature. The optimum available shaping time at each temperature is also shown.

the same experimental set up as for the  $^{55}\text{Fe}$  X-ray and the  $^{241}\text{Am}$  X-ray and  $\gamma$ -ray spectra. The  $^{109}\text{Cd}$  radioisotope X-ray and  $\gamma$ -ray source had an activity of 246 MBq, and again it was encapsulated in a stainless steel capsule with a 250  $\mu\text{m}$  thick Be window. Firstly, spectra were accumulated at 20 °C using each of the pixels, in turn. The spectroscopic response of D1 was then investigated under the illumination of the  $^{109}\text{Cd}$  radioisotope X-ray and  $\gamma$ -ray source as a function of temperature (from 100 °C to 20 °C, in 20 °C steps). For each pixel and temperature, only one spectrum was recorded; an applied reverse bias of 5 V and the optimum available shaping time (as indicated by the results obtained with the  $^{55}\text{Fe}$  radioisotope X-ray source) were used. The live time limit was set to 86,400 s (24 h).

The  $^{109}\text{Cd}$  X-ray and  $\gamma$ -ray spectrum accumulated using D1 at 20 °C can be seen in Fig. 17; similar spectra were collected for the other pixels of the array. The characteristic emissions of the  $^{109}\text{Cd}$  X-ray and  $\gamma$ -ray source [33], the characteristic detector fluorescence peaks, the stainless-steel capsule fluorescence peaks, and escape peaks, were all identified in Fig. 17. Details of the origin of each peak are presented in Table 4.

Gaussians were fitted to the combined Ag  $K\alpha_1$  (22.16 keV) and Ag  $K\alpha_2$  (21.99 keV) photopeak in order to quantify the FWHM at 22.16 keV. The relative emission ratio of the  $^{109}\text{Cd}$  radioisotope X-ray and  $\gamma$ -ray source at 22.16 keV and 21.99 keV (1.9 [33]) and the relative quantum detection efficiency of the pixels at those energies were taken into consideration. The FWHM at 22.16 keV was 830 eV  $\pm$  40 eV for D2, 870 eV  $\pm$  40 eV for D3, and 820 eV  $\pm$  40 eV for both D1 and D4,

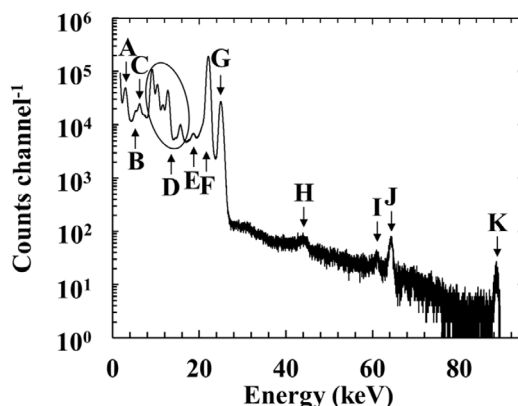


Fig. 17.  $^{109}\text{Cd}$  X-ray and  $\gamma$ -ray spectrum accumulated with D1 at 20 °C (5 V reverse bias and 2  $\mu\text{s}$  shaping time). Details of the major peaks identified can be found in Table 4.

at 20 °C. The mean FWHM at 22.16 keV across all pixels was 840 eV  $\pm$  20 eV (rms error).

A comparison between the  $^{109}\text{Cd}$  X-ray and  $\gamma$ -ray spectra accumulated at the highest (100 °C) and lowest (20 °C) temperatures using D1 is shown in Fig. 18; the number of counts  $\text{keV}^{-1}$  are shown for the convenience of the reader. At each temperature, the FWHM at 22.16 keV was recorded, and the results are shown in Fig. 19; it improved from 1.32 keV  $\pm$  0.06 keV at 100 °C to 0.80 keV  $\pm$  0.04 keV at 20 °C.

Gaussians were also fitted to the detected  $\gamma$ -ray photopeak at 88.03 keV of each  $^{109}\text{Cd}$  X-ray and  $\gamma$ -ray spectrum; the FWHM at 88.03 keV improved from 1.43 keV  $\pm$  0.08 keV at 100 °C to 0.95 keV  $\pm$  0.05 keV at 20 °C. In order to have sufficient number of counts per channel for sufficiently good counting statistics, adjacent channels were combined in a post processing stage while maintaining an appropriate number of channels to ensure that the detected peaks were still adequately sampled and were neither deformed from the detected shape nor in such a way as to affect the measured FWHM [9].

The  $^{241}\text{Am}$  and  $^{109}\text{Cd}$  X-ray and  $\gamma$ -ray spectra were used to subsequently explore the presence of the incomplete charge collection noise (see Section 4.4). The change of the gain of the spectrometer with temperature was also explored and is discussed in Section 4.5.

**Table 4**

Details of the origin of each peak identified in Fig. 17 ( $^{109}\text{Cd}$  X-ray and  $\gamma$ -ray spectrum) [33]. The type of each peak (characteristic emission from the source, CE; fluorescence peak, FP; escape peak, EP; pulse pile up, PP) is also shown for the convenience of the reader.

Peak label Fig. 17	Energy (keV)	Name	Type
A	2.98	Ag $L\alpha$	CE
B	5.4	Cr $K\alpha$ (capsule)	FP
C	6.4	Fe $K\alpha$ (capsule)	FP
D	9.2	Ga $K\alpha$ (detector)	FP
D	10.3	Ga $K\beta$ (detector)	FP
D	10.5	As $K\alpha$ (detector)	FP
D	11.7	As $K\beta$ (detector)	FP
D	10.4–12.9	Ga ( $K\alpha$ , $K\beta$ ) & As ( $K\alpha$ , $K\beta$ ) from Ag $K\alpha_1$	EP
D	10.3–12.7	Ga ( $K\alpha$ , $K\beta$ ) & As ( $K\alpha$ , $K\beta$ ) from Ag $K\alpha_2$	EP
D	13.2–15.7	Ga ( $K\alpha$ , $K\beta$ ) & As ( $K\alpha$ , $K\beta$ ) from Ag $K\beta_1$	EP
D	13.2–15.7	Ga ( $K\alpha$ , $K\beta$ ) & As ( $K\alpha$ , $K\beta$ ) from Ag $K\beta_3$	EP
E	18.4–18.6	In ( $L\beta$ ) from Ag $K\alpha_1$ and Ag $K\alpha_2$	EP
F	21.99	Ag $K\alpha_2$	CE
F	22.16	Ag $K\alpha_1$	CE
G	24.9	Ag $K\beta$	CE
H	44	Ag $K\alpha$	PP
I	60.7	In ( $K\beta$ ) from 88.03 keV	EP
J	63.8	In ( $K\alpha$ ) from 88.03 keV	EP
K	88.03	$\gamma$ -ray	CE

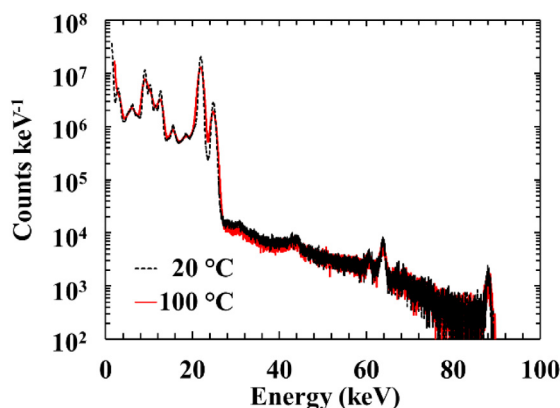


Fig. 18.  $^{109}\text{Cd}$  X-ray and  $\gamma$ -ray spectra obtained with D1 at 100 °C (5 V reverse bias and 1  $\mu\text{s}$  shaping time, —) and 20 °C (5 V reverse bias and 2  $\mu\text{s}$  shaping time, - - -).

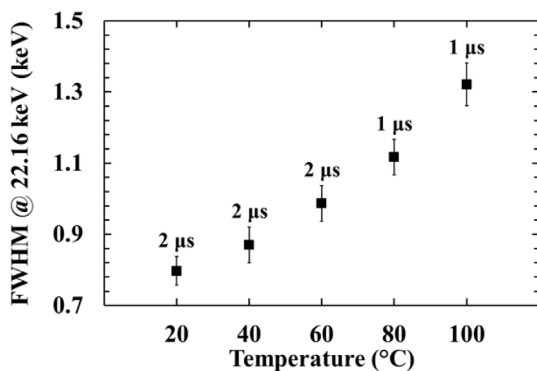


Fig. 19. FWHM at 22.16 keV achieved with D1, as a function of temperature. The optimum available shaping time at each temperature is also shown.

#### 4.4. Investigation of the presence of incomplete charge collection noise

The presence of the incomplete charge collection noise was explored. In a photon counting X/ $\gamma$ -ray spectrometer the electronic noise is independent of photon energy, whereas the incomplete charge collection noise (and Fano noise) varies with photon energy [11]. As such, by subtracting in quadrature the Fano noise from the measured

FWHM at each photon energy, the remainder can be examined for a dependence upon photon energy — such a dependence may be attributed to the presence of detectable incomplete charge collection noise. The absence of an energy dependence in the remainder suggests that the incomplete charge collection noise was negligible across the energy range investigated.

The best FWHM at 5.9 keV, 22.16 keV, 59.54 keV, and 88.03 keV as a function of temperature are summarised in Table 5. The total noise contributions excluding the Fano noise (i.e. the quadratic sum of the electronic and any incomplete charge collection) were calculated at each temperature. As shown in Table 5, subtraction of the Fano noise did indeed result in an energy invariant remainder across the energy range (the rms error of the calculated mean value at each temperature was comparable to/smaller than the uncertainty of the FWHM associated with the Gaussian fitting). It can thus be concluded that the incomplete charge collection noise was negligible in the pixel D1 at every temperature and across the photon energy range when it was operated at an applied reverse bias  $\geq 5$  V. Given the similarity in spectroscopic behaviour of all the pixels at 20 °C and the similarity of the electrical characteristics of all pixels across the temperature range, it is likely that the incomplete charge collection was negligible for every pixel.

Given the absence of the incomplete charge collection in pixel D1 across the temperature range and photon energy range investigated, the contribution of the electronic noise was inferred from Table 5. The quadratic sum of the white parallel noise, white series noise,  $1/f$  noise, and dielectric noise reduced from  $1.29 \text{ keV} \pm 0.02 \text{ keV}$  at 100 °C to  $0.76 \text{ keV} \pm 0.02 \text{ keV}$  at 20 °C. These corresponded to an ENC of  $109 \text{ e}^- \text{ rms} \pm 2 \text{ e}^- \text{ rms}$  (at 100 °C) and  $65 \text{ e}^- \text{ rms} \pm 1 \text{ e}^- \text{ rms}$  (at 20 °C).

#### 4.5. Gain of the spectrometer

The gain of the spectrometer,  $G_S$ , defined here as the number of MCA channels encompassing 1 keV of energy was extracted from the  $^{241}\text{Am}$  and  $^{109}\text{Cd}$  X-ray and  $\gamma$ -ray spectra as functions of temperature; the shaping time and the gain of the shaping amplifier at each temperature were the same for both radioisotope sources.

The centroid channel number of the Gaussians fitted to the 59.54 keV  $\gamma$ -ray peak of the  $^{241}\text{Am}$  X-ray and  $\gamma$ -ray radioisotope source and to the 22.16 keV (Ag  $K\alpha_1$ ) X-ray and the 88.03 keV  $\gamma$ -ray peak of the  $^{109}\text{Cd}$  X-ray and  $\gamma$ -ray radioisotope source were used along with the position of the zero energy noise peak of each accumulated spectrum, to calculate the gain of the spectrometer. The gain of the spectrometer with pixel D1 within the investigated temperature range, as calculated

**Table 5**

Summary of the best FWHM at four energies (5.9 keV, 22.16 keV, 59.54 keV, and 88.03 keV) and the calculated mean FWHM (excluding the Fano noise) across these energies for D1 as a function of temperature,  $T$ .

$T$ (°C)	FWHM (keV) @				Mean FWHM (keV) excl. Fano noise
	5.9 keV	22.16 keV	59.54 keV	88.03 keV	
100 °C	1.29	1.32	1.34	1.43	$1.29 \pm 0.02$
80 °C	1.10	1.12	1.15	1.21	$1.08 \pm 0.01$
60 °C	0.97	0.99	1.00	1.08	$0.94 \pm 0.02$
40 °C	0.86	0.87	0.93	0.99	$0.83 \pm 0.01$
20 °C	0.78	0.80	0.86	0.95	$0.76 \pm 0.02$

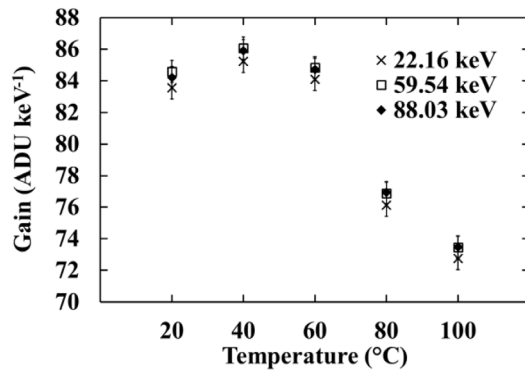


Fig. 20. Gain of the spectrometer as a function of temperature extracted using the Gaussians fitted to three X-ray and  $\gamma$ -ray photopeaks; 22.16 keV ( $\times$ ), 59.54 keV ( $\square$ ), and 88.03 keV ( $\blacklozenge$ ).

using the fitted Gaussians at the three energies, is presented in Fig. 20. The uncertainties of the extracted  $G_S$  resulted from the uncertainties in estimating the centroid channel number of the fitted Gaussians and that of the zero energy noise peak; they were  $\pm 0.7$  ADU keV $^{-1}$  in each case.

At temperatures  $> 40$  °C, the mean gain of the spectrometer decreased, reaching  $73.2$  ADU keV $^{-1} \pm 0.3$  ADU keV $^{-1}$  (rms error) at 100 °C, cf.  $84.1$  ADU keV $^{-1} \pm 0.4$  ADU keV $^{-1}$  (rms error) at 20 °C. However, the rms error of the calculated mean value at each temperature was smaller than the uncertainty of each calculated value of  $G_S$ . As such, it was concluded that the same gain of the spectrometer was calculated using the Gaussians fitted to the three peaks (59.54 keV  $\gamma$ -ray peak, 22.16 keV X-ray peak and 88.03 keV  $\gamma$ -ray peak) for both radioisotope sources (the  $^{241}\text{Am}$  and  $^{109}\text{Cd}$  X-ray and  $\gamma$ -ray radioisotope sources). The gain of the spectrometer was thus exclusively set by its operating conditions (temperature and shaping time and gain of the shaping amplifier); it did not change as the  $^{109}\text{Cd}$  radioisotope X-ray and  $\gamma$ -ray source substituted the  $^{241}\text{Am}$  radioisotope X-ray and  $\gamma$ -ray source. Its temperature variation was attributed to the change of the conversion factor of the preamplifier, since the pixel-preamplifier system was subjected to a temperature range 100 °C – 20 °C. This small but important finding indicates that, since the gain performance of the spectrometer was the same across the energy range investigated and for different radioisotope X-ray and  $\gamma$ -ray sources, any disturbance to the preamplifier electronics and detector array during switching between radioisotope X-ray and  $\gamma$ -ray sources was negligible; as such the results from the different sources may be properly compared with each other as has been reported above.

## 5. Discussion and conclusion

In this article, for the first time, a monolithic  $2 \times 2$  square pixel  $\text{In}_{0.5}\text{Ga}_{0.5}\text{P}$  p $^+$ -i-n $^+$  mesa X-ray and  $\gamma$ -ray photodiode array (pixel size of  $200 \mu\text{m} \times 200 \mu\text{m}$ ; i layer thickness of  $5 \mu\text{m}$ ) has been demonstrated to be spectroscopic at 20 °C; the photon counting X-ray and  $\gamma$ -ray

spectroscopic response of one representative pixel (D1) was also studied at temperatures up to 100 °C.

Comparable leakage currents and capacitances were measured among the pixels. A mean leakage current of  $2.7 \text{ pA} \pm 0.7 \text{ pA}$  (rms error) was measured for the packaged pixels at 15 V applied reverse bias, at 100 °C. The mean depletion layer capacitance of the four pixels at 15 V, within the temperature range 100 °C to 20 °C, was  $0.88 \text{ pF} \pm 0.02 \text{ pF}$  (rms error); the pixels were fully depleted at 5 V.

Each pixel was, in turn, investigated for photon counting X-ray and  $\gamma$ -ray spectroscopy under the illumination of an  $^{55}\text{Fe}$  radioisotope X-ray source, an  $^{241}\text{Am}$  radioisotope X-ray and  $\gamma$ -ray source, and a  $^{109}\text{Cd}$  radioisotope X-ray and  $\gamma$ -ray source. The mean best energy resolution achieved using the pixels at 20 °C was  $770 \text{ eV} \pm 30 \text{ eV}$  (rms error) FWHM at 5.9 keV,  $840 \text{ eV} \pm 20 \text{ eV}$  (rms error) FWHM at 22.16 keV, and  $870 \text{ eV} \pm 30 \text{ eV}$  (rms error) FWHM at 59.54 keV. The pixels had the same FWHM at all investigated energies, within uncertainties.

The spectroscopic response of a representative pixel, D1, was then studied up to a temperature of 100 °C. The FWHM achieved when the array-preamplifier system operating at 100 °C was  $1.29 \text{ keV} \pm 0.04 \text{ keV}$  at 5.9 keV,  $1.32 \text{ keV} \pm 0.06 \text{ keV}$  at 22.16 keV,  $1.34 \text{ keV} \pm 0.06 \text{ keV}$  at 59.54 keV, and  $1.43 \text{ keV} \pm 0.08 \text{ keV}$  at 88.03 keV. The noise analysis of the reported spectroscopic system revealed that the quadratic sum of the dielectric noise and incomplete charge collection noise was the dominant source of noise within the investigated temperature range; it decreased from 100 e $^-$  rms at 100 °C to 59 e $^-$  rms at 20 °C. However, the contribution of the incomplete charge collection noise of pixel D1 at 5 V reverse bias was found to be negligible up to 88.03 keV photon energy and an insignificant change of the incomplete charge collection noise was suggested when the reverse bias increased up to 15 V. It was concluded that the dielectric noise of the  $\text{In}_{0.5}\text{Ga}_{0.5}\text{P}$  pixel D1 itself dominated the total noise at 40 °C and 20 °C, whereas the dielectric noise arising from the feedback capacitance, the passivation and packaging of both the input JFET and the pixel, and any stray dielectrics in close proximity to the input of the preamplifier, dominated the total noise for temperatures  $\geq 60$  °C. The temperature and shaping time and gain of the shaping amplifier was found to establish the gain of the spectrometer.

The presently reported  $\text{In}_{0.5}\text{Ga}_{0.5}\text{P}$  spectrometer had the best energy resolution at 100 °C of any semiconductor pixel array spectrometer reported so far; to the Authors' knowledge, the next best is a GaAs array which had a FWHM at 5.9 keV of  $1.61 \pm 0.04 \text{ keV}$  (166 e $^-$  rms  $\pm 4$  e $^-$  rms) at 100 °C [12].

The results reported are important because they: show an  $\text{In}_{0.5}\text{Ga}_{0.5}\text{P}$  X-ray/ $\gamma$ -ray photodiode array for the first time; extended the energy range used to characterise  $\text{In}_{0.5}\text{Ga}_{0.5}\text{P}$  detectors up to 88.03 keV; and show better high temperature performance than has been achieved with any other photodiode pixel array so far reported. As such,  $\text{In}_{0.5}\text{Ga}_{0.5}\text{P}$  pixel arrays are expected to be of use in novel X-ray and  $\gamma$ -ray spectroscopic imaging systems for a wide variety of applications which benefit from uncooled operation at high temperatures including space science, medical imaging, national security, and defence. Future work is now directed towards the production of larger  $\text{In}_{0.5}\text{Ga}_{0.5}\text{P}$  arrays for photon counting X-ray and  $\gamma$ -ray spectroscopic imagers; it is hoped that such instrumentation will be reported in future publications.

## CRedit authorship contribution statement

**S. Butera:** Methodology, Validation, Formal analysis, Investigation, Data curation, Writing - original draft, Writing - review & editing, Visualization. **G. Lioliou:** Validation, Formal analysis, Data curation, Writing - review & editing, Visualization. **S. Zhao:** Investigation, Data curation, Writing - review & editing. **A.B. Krysa:** Conceptualization, Software, Investigation, Resources, Data curation, Writing - review & editing. **A.M. Barnett:** Conceptualization, Methodology, Validation, Formal analysis, Investigation, Resources, Data curation, Writing - original draft, Writing - review & editing, Visualization, Supervision, Project administration, Funding acquisition.

## Declaration of competing interest

The authors declare that they have no known competing financial interests or personal relationships that could have appeared to influence the work reported in this paper.

## Data availability

Whilst all data from the study and the findings are contained within the paper, further requests for information may be addressed to the authors.

## Acknowledgements

This work was supported by the Science and Technology Facilities Council (STFC), UK, grant ST/R001804/1 (University of Sussex, A.M.B., PI). A.M. Barnett acknowledges funding from the Leverhulme Trust, UK, in the form of a 2016 Philip Leverhulme Prize. The authors are grateful to R. J. Airey and S. Kumar at the EPSRC National Epitaxy Facility for device fabrication. The authors acknowledge N.R. Gemmell for technical computing assistance.

## References

- [1] S. Butera, G. Lioliou, A.B. Krysa, A.M. Barnett, InGaP (GaInP) mesa p-i-n photodiodes for X-ray photon counting spectroscopy, *Sci. Rep.* 7 (2017) 10206.
- [2] S. Butera, G. Lioliou, A.B. Krysa, A.M. Barnett, Temperature characterisation of spectroscopic InGaP X-ray photodiodes, *Nucl. Instrum. Methods Phys. Res. A* 908 (2018) 277–284.
- [3] R.J. Nelson, N. Holonyak Jr, Exciton absorption, photoluminescence and band structure of N-Free and N-DOPED  $\text{In}_{1-x}\text{Ga}_x\text{P}$ , *J. Phys. Chem. Solids* 37 (1976) 629–637.
- [4] C.P. Kuo, S.K. Vong, R.M. Cohen, G.B. Stringfellow, Effect of mismatch strain on band gap in III-V semiconductors, *J. Appl. Phys.* 57 (1985) 5428–5432.
- [5] S. Ozaki, S. Adaki, M. Sato, K. Ohtsuka, Ellipsometric and thermoreflectance spectra of  $(\text{Al}_x\text{Ga}_{1-x})_{0.5}\text{In}_{0.5}\text{P}$  alloys, *J. Appl. Phys.* 79 (1996) 439–445.
- [6] N. Meidinger, J. Eder, T. Eraerds, K. Nandra, D. Pietschner, M. Plattner, A. Rau, R. Strecke, The wide field imager instrument for Athena, *Proc. SPIE* 9905 (2016) 99052A-1-99052A-12.
- [7] Y. Kanemaru, et al., Radiation hardness of a p-channel notch CCD developed for the X-ray CCD camera onboard the XRISM satellite, *J. Instrum.* 14 (2019) C04003.
- [8] J.H. Hubbell, Photon mass attenuation and energy-absorption coefficients, *Int. J. Appl. Rad. Isotopes* 33 (1982) 1269–1290.
- [9] R. Jenkins, R.W. Gould, D. Gedcke, *Quantitative X-Ray Spectrometry*, second ed., CRC Press, New York, 1995.
- [10] A. Owens, M. Bavdaz, A. Peacock, A. Poelaert, H. Andersson, S. Nenonen, H. Sipila, L. Tröger, G. Bertuccio, High resolution X-ray spectroscopy using GaAs arrays, *J. Appl. Phys.* 90 (2001) 5376–5381.
- [11] C. Erd, A. Owens, G. Brammert, M. Bavdaz, A. Peacock, V. Lämsä, S. Nenonen, H. Andersson, N. Haack, Hard X-ray test and evaluation of a prototype  $32 \times 32$  pixel gallium-arsenide array, *Nucl. Instrum. Methods Phys. Res. A* 487 (2002) 78–89.
- [12] G. Lioliou, A.M. Barnett, X-ray and  $\gamma$ -ray spectroscopy using a  $2 \times 2$  GaAs  $\text{p}^+\text{-i-n}^+$  diode array, *Nucl. Instrum. Methods Phys. Res. A* 985 (2021) 164672.
- [13] M.D.C. Whitaker, G. Lioliou, A.M. Barnett,  $\text{Al}_{0.2}\text{Ga}_{0.8}\text{As}$   $2 \times 2$  square pixel X-ray photodiode array, *Nucl. Instrum. Methods Phys. Res. A* 899 (2018) 106–114.
- [14] G. Lioliou, H.K. Chan, T. Gohil, K.V. Vassilevski, N.G. Wright, A.B. Horsfall, A.M. Barnett, 4h-SiC Schottky diode arrays for X-ray detection, *Nucl. Instrum. Methods Phys. Res. A* 840 (2016) 145–152.
- [15] S.M. Sze, K.K. Ng, *Physics of Semiconductor Devices*, third ed., John Wiley & Sons, New Jersey, 2007.
- [16] G.-W. Shu, J.-J. Yang, I.-J. Shu, J.-L. Shen, M.-D. Yang, C.-H. Wu, Y.-S. Huang, Dependence of biasing voltage and illumination power on the built-in electric field of InGaP solar cells, *Japan. J. Appl. Phys.* 51 (2012) 072301.
- [17] G. Bertuccio, P. Rehak, D. Xi, A novel charge sensitive preamplifier without the feedback resistor, *Nucl. Instrum. Methods Phys. Res. A* 326 (1993) 71–76.
- [18] U. Schötzgig, Half-life and X-ray emission probabilities of  $^{55}\text{Fe}$ , *Appl. Radiat. Isot.* 53 (2000) 469–472.
- [19] A.M. Barnett, G. Lioliou, J.S. Ng, Characterization of room temperature AlGaAs soft X-ray mesa photodiodes, *Nucl. Instrum. Methods Phys. Res. A* 774 (2015) 29–33.
- [20] M.D.C. Whitaker, S. Butera, G. Lioliou, A.M. Barnett, Temperature dependence of  $\text{Al}_{0.2}\text{Ga}_{0.8}\text{As}$  X-ray photodiodes for X-ray spectroscopy, *J. Appl. Phys.* 122 (2017) 034501.
- [21] G. Bertuccio, D. Maiocchi, Electron-hole pair generation energy in gallium arsenide by x and  $\gamma$  photons, *J. Appl. Phys.* 92 (2002) 1248–1255.
- [22] G. Bertuccio, A. Pullia, A method for the determination of the noise parameters in preamplifying systems for semiconductor radiation detectors, *Rev. Sci. Instrum.* 64 (1993) 3294–3298.
- [23] G.W. Fraser, *X-ray Detectors in Astronomy*, Cambridge University Press, Cambridge, 1989.
- [24] G. Lioliou, A.B. Krysa, A.M. Barnett, Energy response characterization of InGaP X-ray detectors, *J. Appl. Phys.* 124 (2018) 195704.
- [25] A. Owens, *Compound Semiconductor Radiation Detectors*, CRC Press, Florida, 2012.
- [26] G. Lioliou, A.M. Barnett, Electronic noise in charge sensitive preamplifiers for X-ray spectroscopy and the benefits of a SiC input JFET, *Nucl. Instrum. Methods Phys. Res. A* 801 (2015) 63–72.
- [27] G. Bertuccio, A. Pullia, G. De Geronimo, Criteria of choice of the front-end transistor for low-noise preamplification of detector signals at sub-microsecond shaping times for X- and  $\gamma$ -ray spectroscopy, *Nucl. Instrum. Methods Phys. Res. A* 380 (1996) 301–307.
- [28] E. Gatti, P.F. Manfredi, M. Sampietro, V. Speziali, Suboptimal filtering of  $1/f$ -noise in detector charge measurements, *Nucl. Instrum. Methods Phys. Res. A* 297 (1990) 467–478.
- [29] B.G. Lowe, R.A. Sareen, *Semiconductor X-Ray Detectors*, Taylor & Francis, Group, Boca Raton, 2013.
- [30] G. Bertuccio, R. Casiraghi, Study of silicon carbide for X-ray detection and spectroscopy, *IEEE Trans. Nucl. Sci.* 50 (2003) 175–185.
- [31] H.R. Verma, Measurements of M and L X-ray energies and relative intensities emanating from  $^{241}\text{Am}$  source, *Appl. Radiat. Isot.* 122 (2017) 41–46.
- [32] M.-M. Be, V. Chiste, C. Dulieu, X. Mougeot, E. Browne, V. Chechev, N. Kuzmenko, F. Kondev, A. Luca, M. Galan, A.L. Nichols, A. Arinc, X. Huang, Table of radionuclides ( $a=22$  to  $a=244$ ), *Monographie BIPM-5* 5 (2010).
- [33] H. Xiaolong, Y. Shenggui, D. Chunsheng, Evaluation of the decay data of  $^{109}\text{Cd}$ , *Nucl. Instrum. Methods Phys. Res. A* 621 (2010) 443–446.